

# Broadband X-ray Spectral Study of Nuclear Structure in Local Obscured Radio Galaxies

Yuya Nakatani,<sup>1\*</sup> Yoshihiro Ueda,<sup>1</sup> Claudio Ricci,<sup>2,3</sup> Koki Inaba,<sup>1</sup> Shoji Ogawa,<sup>1,4</sup>  
Kenta Setoguchi,<sup>1</sup> Ryosuke Uematsu,<sup>1</sup> Satoshi Yamada,<sup>5</sup> and Tomohiro Yoshitake<sup>1</sup>

<sup>1</sup>Department of Astronomy, Kyoto University, Kitashirakawa-Oiwake-cho, Sakyo-ku, Kyoto 606-8502, Japan

<sup>2</sup>Instituto de Estudios Astrofísicos, Facultad de Ingeniería y Ciencias, Universidad Diego Portales, Av. Ejército Libertador 441, Santiago, Chile

<sup>3</sup>Kavli Institute for Astronomy and Astrophysics, Peking University, Beijing 100871, People's Republic of China

<sup>4</sup>Institute of Space and Astronautical Science (ISAS), Japan Aerospace Exploration Agency (JAXA) 3-1-1 Yoshinodai, Chuo-ku, Sagami-hara, Kanagawa, Japan

<sup>5</sup>RIKEN Cluster for Pioneering Research, 2-1 Hirosawa, Wako, Saitama 351-0198, Japan

Accepted XXX. Received YYY; in original form ZZZ

## ABSTRACT

Radio galaxies are a key population to understand the importance of relativistic jets in AGN feedback. We present the results of a systematic, broadband X-ray spectral analysis of hard X-ray selected radio galaxies to investigate their nuclear structures. In this study, we focus on the seven most radio-loud, X-ray obscured narrow line radio galaxies in the *Swift*/BAT 70 month AGN catalog. The spectra from 0.5 keV up to 66 keV obtained with *Suzaku* and *NuSTAR* of six objects are newly analyzed here by utilizing the X-ray clumpy torus model (XCLUMPY), whereas we refer to Ogawa et al. (2021) for the results of Centaurus A. We find that these radio galaxies have similar torus covering fractions compared with radio quiet AGNs at the same Eddington ratios ( $-3 < \log \lambda_{\text{Edd}} < -1$ ). This result implies that (1) the torus structure is not an important factor that determines the presence of jets and (2) AGN jets have physically little effect on the torus.

**Key words:** galaxies: active – galaxies: nuclei – galaxies: Seyfert – X-rays: galaxies

## 1 INTRODUCTION

The mass of a supermassive black hole (SMBH) at the center of galaxy and that of its host-galaxy bulge show a tight correlation in the local universe ( $z \sim 0$ ; see Kormendy & Ho 2013 for a review). Such a tight correlation suggests that the central SMBHs and host galaxies have “coevolved” by controlling their respective growths. During the active galactic nucleus (AGN) phase a SMBH gains mass by accretion, which is the dominant channel of the overall SMBH growth over cosmic time (e.g., Marconi et al. 2004; Ueda et al. 2014). To reveal the physical origin of the coevolution, we need to understand how matter is transferred onto SMBHs from galaxy scale (AGN feeding) and how AGNs affect the surrounding environments (AGN feedback; Fabian 2012). The nuclear structure of AGNs, including the “tori” (see e.g., Ramos Almeida & Ricci 2017 for a review), accretion disks, and outflows (jets and winds), can provide us with important clues to solve these fundamental questions.

X-ray observations are a powerful tool to probe into the AGN structure because X-rays have strong penetrating power through dust and gas concealing the central engine, and are sensitive to nearly all material including dust and gas with wide ranges of temperature and ionized stage. In particular, unique information can be obtained through X-ray reflection signatures produced in the circumnuclear material irradiated by the central source (e.g., George & Fabian

1991). This reprocessed radiation is characterized by a hard continuum with a hump at  $\sim 30$  keV and fluorescence lines including the prominent iron  $K\alpha$  line.

Radio galaxies (RGs) are considered to be a key population to understand the importance of relativistic jets in AGN feedback since they could have a significant impact on star formation (e.g., Wagner et al. 2012). One basic question still remains unanswered: are there any distinct differences in the nuclear structure of RGs with respect to radio-quiet AGN, besides the presence or absence of jets? Previous X-ray studies of broad line radio galaxies (BLRGs) suggest that the accretion disks seem to be truncated before reaching to the innermost stable circular orbits (ISCOs; Kataoka et al. 2007; Larsson et al. 2008; Sambruna et al. 2009; Tazaki et al. 2010; Sambruna et al. 2011; Lohfink et al. 2017). This may be different from those of radio-quiet AGNs, where the accretion disks are considered to extend down to the ISCOs in order to produce the relativistically broadened reflection features (e.g., Tanaka et al. 1995). Other models were proposed to interpret these reflection features (e.g., Miyakawa et al. 2012), however, making the comparison non-trivial. Tombesi et al. (2014) performed a systematic search for ultra fast outflows (UFOs) in RGs by utilizing *XMM-Newton* and *Suzaku* data, and estimated that  $50 \pm 20\%$  of RGs show UFOs. Since this fraction is similar to that found in radio-quiet AGNs, the authors concluded that the presence of jets did not preclude that of winds in AGNs.

In this work, we focus on the structures of the tori in RGs and compare them with those of radio-quiet AGNs. The torus is a key element to understand both feeding and feedback mechanisms in an

\* E-mail: nakatani@kusastro.kyoto-u.ac.jp

AGN, since it plays the role of a mass reservoir, spatially connecting the SMBH and its host galaxy. At the same time, the torus could be shaped by feedback from the central engine via disk winds (Elitzur & Shlosman 2006; Fukumura et al. 2010) and via radiation pressure from the central disk (Wada 2015; Ricci et al. 2017b). It is still unclear whether the presence of powerful jets is controlled by, or affects, the torus structure. Previous studies of broadband X-ray spectra of RGs covering energies above 10 keV, focused on constraining their torus structure, are still very limited in sample size (e.g., Tazaki et al. 2011, 2013; Lohfink et al. 2015; LaMassa et al. 2023). In these works, conventional reflection models, such as PEXRAV (Magdziarz & Zdziarski 1995), or so-called “smooth” torus models assuming uniform densities within given boundaries (e.g., Ikeda et al. 2009; Murphy & Yaqoob 2009; Baloković et al. 2018) were employed to model the reflection components. In reality, however, matter distribution in the torus is known to be complex, composed of a clumpy medium. To tackle this issue, Tanimoto et al. (2019) have developed the XCLUMPY model, an X-ray spectral model for a clumpy torus irradiated by an X-ray source, utilizing the Monte Carlo simulation for Astrophysics and Cosmology (MONACO: Odaka et al. 2011, 2016) framework. In XCLUMPY, the clumps are distributed according to power-law and normal profiles in the radial and angular directions, respectively. This model has been successfully applied to the X-ray spectra of a large number of AGNs to constrain the torus geometry (e.g., Miyaji et al. 2019; Tanimoto et al. 2020, 2022; Ogawa et al. 2021; Uematsu et al. 2021; Yamada et al. 2021; Inaba et al. *in prep*).

This paper reports the results of a systematic broadband (0.5–65 keV) X-ray spectral analysis of seven narrow line radio galaxies (NLRGs) in the local universe, utilizing the currently best available data set obtained with *Suzaku* and *NuSTAR*. Our sample is taken from the list of the most radio-loud objects in the *Swift*/BAT 70-month AGN catalog that satisfy the criteria summarized in Section 2. We use the XCLUMPY model to determine the torus geometry of each AGN. Here we newly analyze the spectra of six objects, whereas we refer to Ogawa et al. (2021) for the results of Centaurus A. This is the first work that uniformly applies a clumpy torus model to the X-ray spectra of a statistically well-defined sample of NLRGs. The paper is organized as follows: Section 2 describes the sample selection. Sections 3 and 4 explain the data reduction and X-ray spectral analysis for the six RGs. Their torus properties are discussed in Section 5. Section 6 summarizes the conclusions. In Appendix A, we compare the results of our spectral fitting with those of previous works for the individual objects. Throughout the paper, we adopt the solar abundances of Anders & Grevesse (1989) and assume the following cosmological parameters:  $H_0 = 70 \text{ km s}^{-1} \text{ Mpc}^{-1}$ ,  $\Omega_M = 0.3$ , and  $\Omega_\Lambda = 0.7$ . Errors on the spectral parameters correspond to 90% confidence limits for a single parameter of interest, unless otherwise stated.

## 2 SAMPLE SELECTION

Our sample finally consists of seven NLRGs selected from the *Swift*/BAT 70-month AGN catalog<sup>1</sup> (Baumgartner et al. 2013) by the following criteria.<sup>2</sup> To select the most radio-loud AGNs in the parent *Swift*/BAT sample, we first excluded all blazars, and then set a lower-limit to the radio loudness parameter,  $\log R > -2.8$ , where

<sup>1</sup> <http://swift.gsfc.nasa.gov/results/bs70mon/>

<sup>2</sup> We exclude Cygnus A from our sample, to avoid uncertainties in the spectral modeling due to the large contamination from the intracluster medium (Reynolds et al. 2015), although it satisfies the selection criteria.

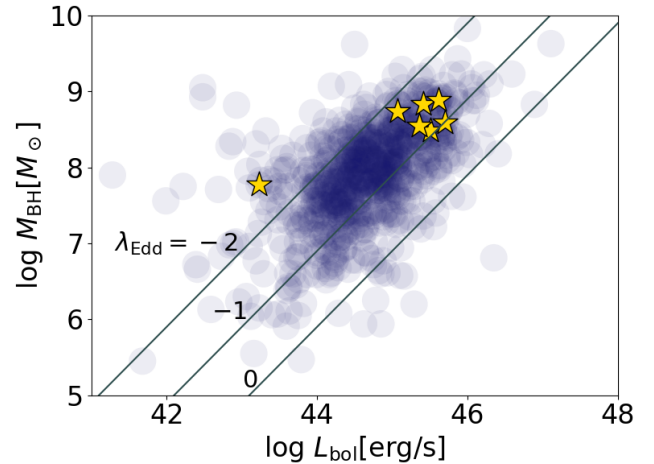


**Figure 1.** Relation of  $M_{\text{BH}}$  and  $L_{\text{bol}}$  reported in (Koss et al. 2022) for our sample (yellow stars; the left-most one is Centaurus A) and for the whole *Swift*/BAT 70-month sample (blue circle). Blazars are excluded. The black lines correspond to constant Eddington-ratio lines:  $\log \lambda_{\text{Edd}} = -2, -1, \text{ and } 0$ .

$R$  is defined as the ratio between the 1.4 GHz flux  $\nu f_\nu(1.4\text{GHz})$  in units of mJy Hz ( $f_\nu$  is the flux density at the frequency  $\nu$ ) and the intrinsic 14–150 keV flux  $f_{14-150\text{keV}}$  in units of  $\text{J m}^{-2} \text{ s}^{-1}$  [ $R \equiv \log(\nu f_\nu(1.4\text{GHz})/f_{14-150\text{keV}})$ ]. The radio-loudness was estimated for the AGN from the *Swift*/BAT 70-month catalogue by considering literature values for their total 1.4 GHz emission from the core and jets/lobes. For most of the sources these values were taken from the NRAO VLA Sky Survey (NVSS; Condon et al. 1998) or from the Green Bank 1.4 GHz Northern Sky Survey (White & Becker 1992). For the sources of our sample, the 1.4 GHz fluxes we used were reported by the Green Bank survey (VII Zw 292, 3C 403, 3C 105, 3C 452; White & Becker 1992), by NVSS (Condon et al. 1998 for PKS 0326–288 and Kuźmicz et al. 2018 for PKS 2356–61), and by a VLA observation (Centaurus A; Condon et al. 1996). The intrinsic 14–150 keV flux were taken from Ricci et al. (2017a).

We further limit our sample to X-ray obscured AGNs with line-of-sight absorption  $\log(N_{\text{H}}^{\text{LOS}}/\text{cm}^{-2}) > 23$ , where  $N_{\text{H}}^{\text{LOS}}$  was obtained by Ricci et al. (2017a). This is because (1) we can more reliably determine the torus parameters in heavily obscured AGNs than in unobscured AGNs by utilizing information of the line-of-sight absorption (Ogawa et al. 2021) and (2) the contribution of emissions from the relativistic jets in the observed X-ray spectra is much smaller in edge-on cases (obscured AGNs) than in face-on cases (unobscured AGNs) assuming that such jets are perpendicular to the torus equatorial plane (see Section 5.3). The lower threshold for  $N_{\text{H}}^{\text{LOS}}$  is also applied to ensure that the absorption is caused by torus matter, not by interstellar medium in the host galaxy. We finally require that the objects were observed with *NuSTAR* to utilize high-quality hard X-ray spectra above 10 keV. The basic information of our sample is listed in Table 1.

Figure 1 shows the relation between the black hole mass  $M_{\text{BH}}$  and the bolometric luminosity  $L_{\text{bol}}$  for our sample and the total *Swift*/BAT 70-month AGN sample. As noticed, the six objects other than Centaurus A (left-most object) are distributed in a narrow region on this plane, having relatively large black hole masses ( $\log M_{\text{BH}}[M_\odot] = 8 - 9$ ) and bolometric luminosities ( $\log L_{\text{bol}}[\text{ergs/s}] = 45 - 46$ ) compared with the parent sample. They show Eddington ratios of  $-2 < \log \lambda_{\text{Edd}} < -1$ .

**Table 1.** Summary of Objects.

(1) Galaxy name. (2) Swift source name. (3) Redshift from the NASA/IPAC Extragalactic Database (NED; <https://ned.ipac.caltech.edu/>). (4) total Galactic  $H I$  and  $H_2$  values in units of  $10^{22} \text{ cm}^{-2}$  (Willingale et al. 2013). (5) Radio loudness defined as the ratio between the 1.4 GHz flux and the intrinsic 14–150 keV flux. (6) Radio AGN classification from the NED. (7) 1.4 GHz flux density in units of mJy. (8) logarithmic column density along the line-of-sight in units of  $\text{cm}^{-2}$  (Ricci et al. 2017a). (9) References of column (3), (6), and (7). “...” denotes no reference.

**References.** (B) Bottinelli et al. (1992); (C96) Condon et al. (1996); (C98) Condon et al. (1998); (H) Hardcastle et al. (1999); (J) Jones et al. (2009); (Ki) Kim et al. (2021); (Ku) Kuźmicz et al. (2018); (L) Loveday et al. (1996); (O) Owen & Laing (1989); (R) Ricci et al. (2017a); (S) Spinrad et al. (1985); (W) White & Becker (1992)

(1) Object	(2) Swift ID	(3) Redshift	(4) $N_{\text{H}}^{\text{Gal}}$	(5) Radio loudness	(6) Radio Class	(7) Radio flux	(8) $\log N_{\text{H}}^{\text{LOS}}$	(9) Ref
PKS 0326–288	SWIFT J0328.4-2846	0.10877	0.0102	-2.8	...	1450	23.82	(J,...,C98)
VII Zw 292	SWIFT J0950.5+7318	0.0581	0.0233	-2.69	FR II	2653	23.79	(R,O,W)
3C 403	SWIFT J1952.4+0237	0.0584	0.195	-2.69	FR II	5798	23.69	(Ki,H,W)
3C 105	SWIFT J0407.4+0339	0.089	0.22	-2.63	FR II	5339	23.75	(S,H,W)
Centaurus A	SWIFT J1325.4-4301	0.00183	0.117	-2.51	...	278000	23.02	(B,...,C96)
3C 452	SWIFT J2246.0+3941	0.0811	0.144	-2.33	FR II	10197	23.76	(R,H,W)
PKS 2356–61	SWIFT J2359.3-6058	0.09631	0.0157	-1.52	...	26240	23.16	(L,...,Ku)

### 3 OBSERVATIONS AND DATA REDUCTION

Table 2 summarizes the *Suzaku* and *NuSTAR* data of the six RGs (other than Centaurus A) analyzed here. The data reduction was conducted in accordance with the procedures described below.

#### 3.1 *Suzaku*

*Suzaku* (Mitsuda et al. 2007) carried four X-ray CCD cameras called the X-ray Imaging Spectrometers (XISs), which were sensitive to X-rays in the 0.2–12 keV range. XIS0, XIS2, and XIS3 were frontside-illuminated CCD cameras (XIS-FI), and XIS1 was backside-illuminated one (XIS-BI). *Suzaku* also carried the hard X-ray detector (HXD), a non-imaging instrument consisting of p-i-n type silicon photodiodes (hereafter PIN) and gadolinium silicate [ $\text{Gd}_2\text{SiO}_5(\text{Ce})$ ] phoswich counters (hereafter GSO), which were sensitive to hard X-rays with energies of 10–70 keV and 40–600 keV, respectively. In this work, we only utilize HXD-PIN data because our targets were too faint to be detected with HXD-GSO.

The *Suzaku*/XIS data were reduced by using the latest versions of the calibration database (CALDB) released on 2018 October 10 and HEASoft v6.30.1 packages. We accumulated photon events in circular regions around the target with radii of 1–2 arcmin, depending on the source flux. The background spectra were extracted from circular regions with radii of 1.5–4 arcmin that were free of any obvious point sources. The response matrix files (RMFs) and ancillary response files (ARFs) were generated with the XISRMFGEN and XISSIMARFGEN tools (Ishisaki et al. 2007), respectively. We combined the spectra and responses of XIS-FI using the ADDASCASPEC script. The spectral bins were merged to contain at least 25 photons per each bin in order to facilitate the use of  $\chi^2$ -statistics.

The HXD-PIN data were reduced by using the AEPIPELINE script. For background subtraction we used the “tuned” non X-ray background (NXB) event files (Fukazawa et al. 2009) to produce the NXB spectra, to which simulated cosmic X-ray background (CXB) spectrum were added. In the spectral analysis, we utilized only the energy range within 16–40 keV where the source flux is brighter than 3% of the NXB level (the maximum systematic error in the 15–70 keV range; Fukazawa et al. 2009).

#### 3.2 *NuSTAR*

*NuSTAR* (Harrison et al. 2013) carries two focal plane modules (FPMs: FPMA and FPMB). The FPMs, coupled with the multilayer coated hard X-ray mirrors, are sensitive to X-ray energies of 3–79 keV. The FPMs data were reprocessed by using HEASoft v6.30.1 with CALDB version 20200429. The source spectra were extracted by considering circles with radii of 90–120 arcsec (depending on the flux) centered on the target. The background spectra were extracted from source-free circular regions with radii of 90–120 arcsec. The response matrix files (RMFs) and the ancillary response files (ARFs) were generated with the NUPRODUCTS script. We combined the spectra and responses of the two FPMs by using ADDASCASPEC to achieve the highest signal-to-noise ratios in a single spectrum; we confirmed that consistent results were obtained by fitting the FPMA and FPMB spectra separately. For the case of 3C 105, we also combined the spectra of the three observations spanning over 2 days (Table 2). Considering the lower energy resolution of *NuSTAR*/FPMs than *Suzaku*/XIS and the absence of sharp spectral features above 8 keV we use (see Section 4), we combined the spectral bins to contain at least 30 photons per bin (cf. 25 photons per bin for *Suzaku*/XIS), in order to increase the sensitivities for continuum determination.

### 4 X-RAY SPECTRAL ANALYSIS

We simultaneously fit the broadband spectra of each object taken with *Suzaku*/XIS-FI (0.5–10 keV), *Suzaku*/XIS-BI (0.5–9 keV), *Suzaku*/HXD-PIN (16–40 keV), and *NuSTAR*/FPMs (8–66 keV; for the sources for which it was possible to have the widest spectral coverage)<sup>3</sup>. Conservatively, we decide not to use the *NuSTAR* data below 8 keV, considering the possible cross-calibration uncertainties in the energy-dependent effective area with other instruments at energies below 6–8 keV (see e.g., Appendix 3 of Diez et al. 2023). Spectral fitting is performed on XSPEC (Arnaud 1996) v12.12.1 based on  $\chi^2$ -statistics.

<sup>3</sup> We do not include the HXD-PIN spectra for PKS 0326–288 and 3C 452 in the fitting, considering the poor signal-to-noise ratios and possible contamination by nearby sources, respectively.

**Table 2.** Summary of X-ray Observations. Exposures are based on the good time intervals of XIS 0 for *Suzaku* and those of FPMA for *NuSTAR*.

Object	Observatory	ObsID	Start Date (UT)	End Date (UT)	Exposure (ks)
PKS 0326–288	<i>Suzaku</i>	704039010	2010 Jan 30 21:20	2010 Feb 01 07:50	58
	<i>NuSTAR</i>	60160155002	2020 Jan 26 07:56	2020 Jan 26 18:51	22
VII Zw 292	<i>Suzaku</i>	703018010	2008 Nov 16 22:10	2008 Nov 18 11:52	81
	<i>NuSTAR</i>	60160374002	2016 Dec 05 02:51	2016 Dec 05 09:06	13
3C 403	<i>Suzaku</i>	704011010	2009 Apr 08 19:53	2009 Apr 10 02:35	48
	<i>NuSTAR</i>	60061293002	2013 May 25 18:06	2013 May 26 05:01	20
3C 105	<i>Suzaku</i>	702074010	2008 Feb 05 12:52	2008 Feb 07 02:00	38
	<i>NuSTAR</i>	60061044002	2013 Feb 15 02:06	2013 Feb 15 04:51	5
	<i>NuSTAR</i>	60061044004	2013 Feb 15 15:01	2013 Feb 15 18:01	6
	<i>NuSTAR</i>	60061044006	2013 Feb 16 03:56	2013 Feb 16 06:36	6
3C 452	<i>Suzaku</i>	702073010	2007 Jun 16 09:30	2007 Jun 17 19:54	67
	<i>NuSTAR</i>	60261004002	2017 May 01 00:56	2017 May 02 03:51	51
PKS 2356–61	<i>Suzaku</i>	801016010	2006 Dec 06 17:08	2006 Dec 09 05:11	101
	<i>NuSTAR</i>	60061330002	2014 Aug 10 17:16	2014 Aug 11 05:06	23

#### 4.1 Spectral Model

For consistency with previous works on radio-quiet AGNs utilizing the XCLUMPY model (e.g., Tanimoto et al. 2020; Ogawa et al. 2021; Inaba et al, *in prep*), we adopt basically the same spectral model as used in these papers. Our model represents a typical X-ray spectrum of an obscured AGN, consisting of a direct power-law component absorbed by material in the line of sight, reflection components from the torus, and an unabsorbed scattered component by optically thin matter (most likely by an ionized gas in the polar region). In many cases, we also add optically-thin thermal emission from the host galaxy that is seen low energies below  $\sim 2$  keV. The model is expressed as follows in XSPEC terminology:

$$\begin{aligned}
 \text{Model} &= \text{const1} * \text{phabs} \\
 &* (\text{zphabs} * \text{cabs} * \text{const2} * \text{zcutoffpl}) \\
 &+ \text{atable}\{\text{xclumpy\_RC.fits}\} \\
 &+ \text{atable}\{\text{xclumpy\_RL.fits}\} \\
 &+ \text{const3} * \text{zcutoffpl} \\
 &+ \text{apec}
 \end{aligned}$$

(1) The `const1` term represents an instrumental cross-calibration constant among different detectors. We set `const1` of *NuSTAR*/FPM to 1 as a reference, and fix those of *Suzaku*/XIS-FI and *Suzaku*/HXD at 0.95 and 1.12, respectively, based on the results obtained by Madsen et al. (2017). We allow that of *Suzaku*/XIS-BI to be free. The `phabs` term represents the Galactic absorption, whose hydrogen column density ( $N_{\text{H}}^{\text{Gal}}$ ) is fixed at the total value of  $H\text{I}$  and  $H_2$  based on <https://www.swift.ac.uk/analysis/nhtot/> (Willingale et al. 2013).

(2) The `zcutoffpl` term, a power law with a high energy cutoff, represents the direct component. We fix the cutoff energy at a typical value ( $E_{\text{cut}} = 370$  keV: Ricci et al. 2018), since it would be difficult to constrain from our data. The `zphabs*cabs` term accounts for the photoelectric absorption and Compton scattering by line-of-sight material, whose hydrogen column density is determined by equation 1. The `const2` term is a constant to deal with time variability between the *NuSTAR* and *Suzaku* observations. We fix that of *NuSTAR* at unity as a reference, and allow that of *Suzaku* free. Here we implicitly assume that the spectral shape is constant between the different observation epochs. Indeed, by separately analyzing the *Suzaku* and *NuSTAR* spectra at energies above 8 keV (commonly covered by the two satellites) with a simple absorbed power-law model, we con-

firmed that the spectral parameters did not vary over the statistical errors. It is also supported by the absence of any systematic residuals in the simultaneous fit of the *Suzaku* and *NuSTAR* spectra (Figure 2).

(3) The two tables of XCLUMPY, `atable{xclumpy_RC.fits}` and `atable{xclumpy_RL.fits}`, which correspond to the reflection continuum and emission line components, respectively. The free parameters of XCLUMPY are the hydrogen column density along the equatorial plane ( $N_{\text{H}}^{\text{Equ}}$ ), the torus angular width ( $\sigma$ ), and the inclination angle ( $i$ ). Considering that all targets show large line-of-sight absorption, we limit the inclination to a range between  $60^\circ$  and  $87^\circ$  (the hard limit in the table models). For 3C 105, we fix it at  $i = 70^\circ$ , since it cannot be constrained by our data. The photon index, normalization, and cutoff energy are linked to the values of the direct component. The hydrogen column density along the line of sight ( $N_{\text{H}}^{\text{LOS}}$ ) in (2) is calculated from the torus parameters as follows:

$$N_{\text{H}}^{\text{LOS}}(\theta) = N_{\text{H}}^{\text{Equ}} \exp\left(-\left(\frac{90^\circ - i}{\sigma}\right)^2\right). \quad (1)$$

Considering the large size of the torus ( $\sim \text{pc}$ ), we assume that the flux of the torus reflection component remained constant among the different observation epochs.

(4) The `const3` factor gives the scattering fraction ( $f_{\text{scat}}$ ). The parameters of `zcutoffpl` are linked to those of the direct component. We limit  $f_{\text{scat}}$  within a range of 0.0–10 %.

(5) The `apec` term represents optically-thin thermal emission from the host galaxy, which is added when required by the data.

#### 4.2 Results

We find that this model can fairly reproduce the observed broadband spectra of all objects ( $\chi_{\text{red}}^2 \equiv \chi^2/\text{d.o.f} < 1.2$ ). The best-fit parameters are summarized in Table 3. The observed spectra folded with the energy responses (corrected for effective area) are plotted in the left column of Figure 2, where the best-fit models are overplotted together with the fitting residuals (lower panels). In the right column of Figure 2, we plot the multi-component best-fit models in units of  $E \times I(E)$  (where  $I(E)$  is the energy flux density at the energy  $E$ ). Table 4 lists the intrinsic (de-absorbed) 2–10 keV luminosities of the direct components obtained from our spectral fitting, together with

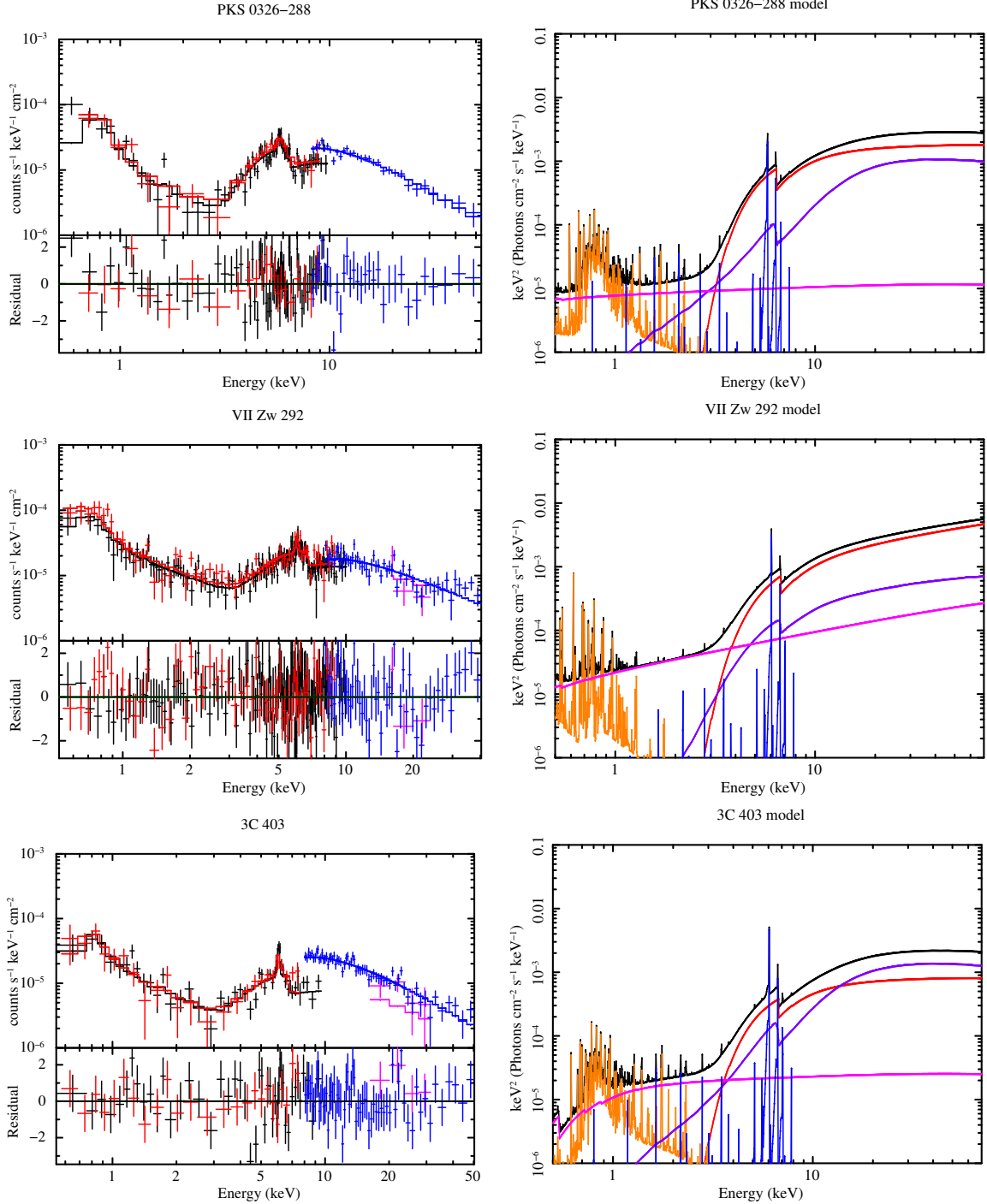


**Figure 2.** Left: (upper panels) Observed X-ray spectra folded with the energy responses (but corrected for effective area): *Suzaku*/XIS-FI (black crosses), *Suzaku*/XIS-BI (red crosses), *Suzaku*/HXD-PIN (magenta crosses), and *NuSTAR*/FPMs (blue crosses). The best-fit models are overlotted by the lines. (lower panels) Fitting residuals in units of  $1\sigma$  error. Right: The best-fit models in units of  $E \times I_E$  (where  $I_E$  is the energy flux at the energy  $E$ ). The solid lines show the total (black), direct component (red), reflection continuum from the torus (purple), emission lines from the torus (blue), scattered component (magenta), and soft excess (orange).

the black hole masses and Eddington ratios taken from [Koss et al. \(2022\)](#)<sup>4</sup>.

<sup>4</sup> Throughout the paper, we adopt the Eddington ratio values in ([Koss et al. 2022](#)), which were obtained from the 105-month averaged *Swift*/BAT data, in order to minimize the effect of time variability.

## 5 DISCUSSION

### 5.1 Properties of Local Obscured Radio Galaxies

For our study, we have constructed a new sample of nearby X-ray obscured NLRGs consisting of the seven most radio-loud AGNs with absorption of  $\log(N_{\text{H}}^{\text{LOS}}/\text{cm}^{-2}) > 23$  in the *Swift*/BAT 70-month

**Table 3.** Best Fit Parameters.

(1) Galaxy name. (2) Logarithmic observed flux in  $\text{ergs cm}^{-2} \text{s}^{-1}$ , in the range of 2–10 keV (*Suzaku*/XIS-FI). (3) Photon index of the direct component, and the normalization in  $10^{-3}$  photons  $\text{keV}^{-1} \text{cm}^{-2} \text{s}^{-1}$  at 1 keV. (4) Temperature of the *apec* model in keV and its normalization of the *apec* model in  $10^{-19}/4\pi[D_A(1+z)]^2 \int n_e n_H dV$ , where  $D_A$  is the angular diameter distance to the source in cm,  $n_e$  and  $n_H$  are the electron and hydrogen densities in  $\text{cm}^{-3}$ , respectively. (5) Hydrogen column density along the equatorial plane in  $10^{24} \text{cm}^{-2}$ , torus angular width in degree, inclination angle of the observer in degree, and hydrogen column density along the line of sight in  $10^{22} \text{cm}^{-2}$ . (6) Time variability constant (relative normalization of *Suzaku*/XIS to *NuSTAR*/FPMs) and instrumental cross-calibration constant of *Suzaku*/XIS-BI against *Suzaku*/XIS-FI. (7) Scattering fraction in %.

† - The parameter has reached its limit of its allowed range. ‡ - The parameter has been fixed at  $70^\circ$ .

(1) Object	(2) $\log F_{2-10\text{keV}}$	(3) zcutoffpl $\Gamma$ $N_{\text{pow}}$	(4) apec $kT$ $N_{\text{apec}}$	(5) XCLUMPY $N_{\text{H}}^{\text{Equ}}$ $\sigma$ $i$ $N_{\text{H}}^{\text{LOS}}$	(6) const2 $C_{\text{TIME}}$ $C_{\text{BI}}$	(7) const3 $f_{\text{scat}}$	$\chi^2/\text{d.o.f.}$
PKS 0326–288	-12.0	$1.74^{+0.13}_{-0.14}$ $3.0^{+1.42}_{-1.07}$	$0.79^{+0.15}_{-0.17}$ $1.25^{+0.32}_{-0.31}$	$1.2^{+8.8\dagger}_{-0.7}$ $10.0^{+8.92}_{-0.0\dagger}$ $80.69^{+6.31\dagger}_{-16.21}$ $49.7^{+3.5}_{-6.79}$	$0.56^{+0.07}_{-0.07}$ $1.09^{+0.1}_{-0.09}$	$0.38^{+0.2}_{-0.15}$	136.22/119
VII Zw 292	-11.95	$1.36^{+0.14}_{-0.13}$ $0.79^{+0.43}_{-0.27}$	$0.29^{+0.11}_{-0.05}$ $2.28^{+0.96}_{-0.92}$	$0.42^{+0.98}_{-0.05}$ $26.08^{+14.54}_{-14.49}$ $87.0^{+0.0\dagger}_{-19.26}$ $41.14^{+2.71}_{-2.49}$	$0.74^{+0.11}_{-0.09}$ $1.11^{+0.07}_{-0.07}$	$3.36^{+1.44}_{-1.02}$	300.25/264
3C 403	-12.17	$1.87^{+0.19}_{-0.24}$ $4.08^{+3.86}_{-2.14}$	$0.73^{+0.15}_{-0.19}$ $1.85^{+0.61}_{-0.57}$	$5.62^{+4.38\dagger}_{-4.85}$ $14.46^{+4.43}_{-4.46\dagger}$ $66.89^{+10.06}_{-6.89\dagger}$ $43.65^{+7.1}_{-6.71}$	$0.22^{+0.04}_{-0.05}$ $1.03^{+0.13}_{-0.12}$	$0.51^{+0.48}_{-0.24}$	152.23/130
3C 105	-11.68	$1.48^{+0.12}_{-0.12}$ $0.9^{+0.39}_{-0.22}$	... ...	$0.41^{+0.19}_{-0.04}$ $89.59^{+0.41\dagger}_{-57.58}$ $70.0^\ddagger$ $39.27^{+2.97}_{-3.58}$	$1.72^{+0.18}_{-0.18}$ $1.07^{+0.09}_{-0.09}$	$1.7^{+0.47}_{-0.55}$	103.17/113
3C 452	-11.69	$1.61^{+0.06}_{-0.07}$ $3.32^{+0.79}_{-0.76}$	$1.22^{+0.7}_{-0.78}$ $1.34^{+2.17}_{-1.03}$	$0.44^{+1.11}_{-0.04}$ $22.11^{+6.04}_{-9.39}$ $86.63^{+0.37\dagger}_{-15.56}$ $43.39^{+2.24}_{-5.78}$	$0.5^{+0.05}_{-0.04}$ $1.02^{+0.05}_{-0.05}$	$2.79^{+0.68}_{-0.45}$	192.64/230
PKS 2356–61	-11.45	$1.58^{+0.05}_{-0.01}$ $1.03^{+0.14}_{-0.05}$	$0.16^{+0.05}_{-0.15}$ $2.49^{+3.92}_{-1.14}$	$0.27^{+0.86}_{-0.14}$ $24.14^{+65.86\dagger}_{-6.56}$ $70.09^{+16.91\dagger}_{-5.05}$ $13.64^{+0.36}_{-0.34}$	$1.44^{+0.06}_{-0.09}$ $1.07^{+0.03}_{-0.03}$	$10.0^{+0.0\dagger}_{-1.27}$	339.1/306

**Table 4.** AGN key parameters.

(1) Galaxy name. (2) Logarithmic black hole mass in  $M_\odot$  (Koss et al. 2022). (3) Logarithmic Eddington ratio (Koss et al. 2022) based on the 105-month averaged Swift/BAT luminosity. (4) Logarithmic intrinsic 2–10 keV luminosity of the direct component in  $\text{erg s}^{-1}$  derived from our spectral analysis. (5) Torus covering fraction.

(1) Object	(2) $\log M_{\text{BH}}/M_\odot$	(3) $\log \lambda_{\text{Edd}}$	(4) $\log L_{2-10\text{keV}}$	(5) $C_{\text{T}}$
PKS 0326–288	8.48	-1.14	44.49	$0.37^{+0.27}_{-0.03}$
VII Zw 292	8.74	-1.84	43.6	$0.77^{+0.21}_{-0.32}$
3C 403	8.83	-1.59	43.97	$0.59^{+0.14}_{-0.23}$
3C 105	8.59	-1.07	43.94	$1.0^{+0.0}_{-0.1}$
3C 452	8.89	-1.46	44.33	$0.68^{+0.16}_{-0.23}$
PKS 2356–61	8.55	-1.36	43.99	$0.69^{+0.31}_{-0.14}$

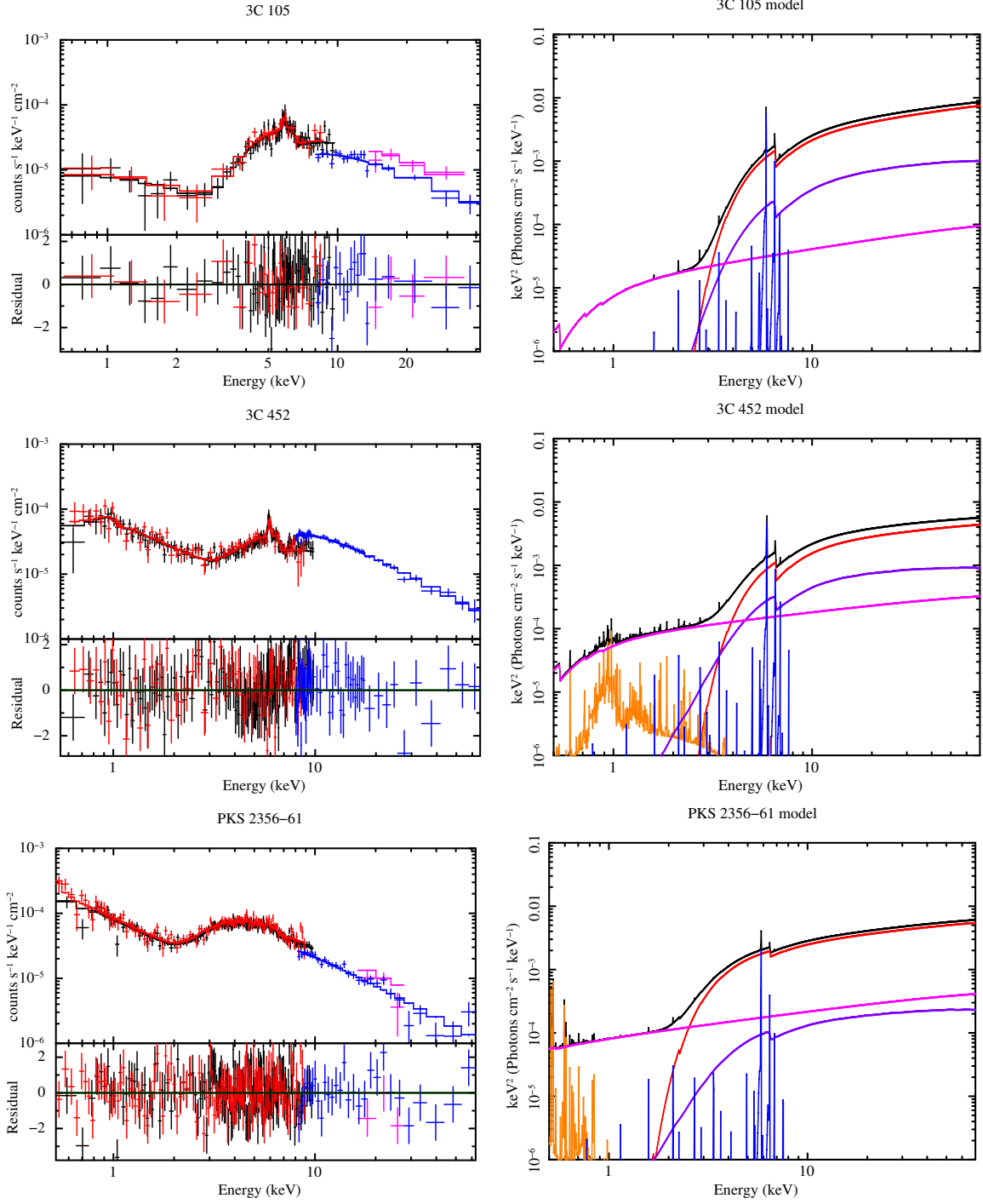


Figure 2. Continued.

AGN (non-blazar) catalog. Most of them are classified as Fanaroff-Riley (FR) II RGs (Table 1), which have stronger jet power than FR I RGs (Fanaroff & Riley 1974). We have adopted the radio-to-X-ray radio loudness parameter  $R \equiv \log(\nu f_{\nu}(1.4\text{GHz})/f_{14-150\text{keV}}) > -2.8$ , which is free from AGN obscuration and contamination by the host galaxy emission; these are advantages to obtain a “clean” radio-loud AGN sample over radio loudness parameters defined between radio and optical fluxes (Terashima & Wilson 2003). Our sample is selected with well-defined criteria (Section 2) except for the availability of

high-quality hard band data taken with *NuSTAR*, and hence can be regarded as a representative sample of local obscured RGs with strong jets.

As mentioned in Section 2, most of our sample (except Centaurus A) has limited ranges of the bolometric luminosity ( $45 < \log L_{\text{bol}}/(\text{ergs}^{-1}) < 46$ ) and Eddington ratio ( $-2 < \log \lambda_{\text{Edd}} < -1$ ). Due to the small size of our sample, it is not clear whether the most powerful jets in AGNs can be selectively produced at specific conditions on luminosity or Eddington ratio; quantitative comparison of

luminosity or Eddington ratio distribution between radio-loud and radio-quiet AGNs is out of the scope of this paper and is left for a future work. Nevertheless, since these values of  $\log L_{\text{bol}}$  and  $\lambda_{\text{Edd}}$  are typical of *Swift*/BAT AGNs (mostly radio-quiet ones), it is suggested that the launching mechanisms of jets are not controlled solely by the mass accretion rate in the accretion disk (luminosity) or that normalized by the black hole mass (Eddington ratio). This is consistent with the presence of two distinct sequences in the Eddington ratio versus radio loudness plane found for radio- or optically-selected AGNs (Sikora et al. 2007).

## 5.2 Torus Covering Fraction as a Function of Eddington Ratio

We have analyzed the currently available highest-quality broadband X-ray spectra of six RGs obtained with *Suzaku* and *NuSTAR* in the 0.5–66 keV band. To study the X-ray reprocessed radiation from the torus, we have employed one of the latest X-ray clumpy models, XCLUMPY (Tanimoto et al. 2019). In this subsection, we discuss the torus geometry of our RGs in terms of the covering fraction  $C_{\text{T}}$ , defined as the solid angle of the torus matter with column densities of  $\log N_{\text{H}}/\text{cm}^{-2} > 22$  normalized by  $4\pi$ .

By measuring absorbed AGN fractions in the *Swift*/BAT AGN sample, which is dominated by radio-quiet AGNs, Ricci et al. (2017b) find that the torus covering fraction is determined mainly by the Eddington ratio, not by the luminosity of the AGN (see also Ricci et al. (2022) for an updated view). Since  $C_{\text{T}}$  shows a rapid drop at  $\log \lambda_{\text{Edd}} \gtrsim -1.5$ , they conclude that obscuring matter in an AGN is located within the sphere of influence by the SMBH and the torus is shaped by radiation pressure of the AGN on dusty gas. Utilizing the best-fit torus parameters of XCLUMPY, it is also possible to calculate  $C_{\text{T}}$  of an individual object as follows (Ogawa et al. 2021):

$$C_{\text{T}} = \sin\left(\sigma \sqrt{\ln\left(\frac{N_{\text{H}}^{\text{Equ}}}{10^{22} \text{ cm}^{-2}}\right)}\right). \quad (2)$$

Ogawa et al. (2021) and Inaba et al. (*in prep*) confirm that the covering fractions of radio-quiet AGNs determined through X-ray spectroscopy follow well the Ricci et al. (2017b) relation between  $C_{\text{T}}$  and  $\log \lambda_{\text{Edd}}$ .

Table 4 lists the  $C_{\text{T}}$  values for our RG sample. The result for Centaurus A is taken after Ogawa et al. (2021). Figure 3 plots  $C_{\text{T}}$  as a function of  $\lambda_{\text{Edd}}$  (taken from Koss et al. 2022); here we exclude 3C 105 where the torus widths ( $\sigma$ ) is almost unconstrained by our data even when the inclination is fixed. We estimate the errors of  $C_{\text{T}}$  by fully considering the parameter coupling among the torus parameters; we first make the error contour map on the  $N_{\text{H}}^{\text{Equ}}$  versus  $\sigma$  plane and then find the error region of  $C_{\text{T}}$  by comparing the contours with constant  $C_{\text{T}}$  lines on the plane.

As noticed from the figure, our results for the individual objects are mostly consistent with the relation by Ricci et al. (2017b). The mean value of the covering fractions for the five objects at  $-2 < \log \lambda_{\text{Edd}} < -1$  is found to be  $\bar{C}_{\text{T}} = 0.62 \pm 0.08$ . This is similar to the average of radio-quiet AGNs at the same range of  $\log \lambda_{\text{Edd}}$  obtained by Inaba et al. (*in prep*),  $\bar{C}_{\text{T}} = 0.62 \pm 0.02$ . Centaurus A shows  $C_{\text{T}} = 0.995^{+0.005}_{-0.057}$  at  $\log \lambda_{\text{Edd}} = -2.7$ , which agrees with the Ricci et al. (2017b) curve.

At even lower Eddington ratios, we refer to the Hitomi result of the radio galaxy NGC 1275 (Hitomi Collaboration et al. 2018), whose Eddington ratio is estimated to be  $\log \lambda_{\text{Edd}} = -3.6$  (Sikora et al. 2007). On the basis of the narrow and weak iron-K $\alpha$  line, the authors concluded that the torus in NGC 1275 has only a small solid angle. This trend is also seen in the total *Swift*/BAT AGN sample (Ricci

et al. 2017b), and is consistent with the spectral analysis results of local low-luminosity AGNs (e.g., Kawamuro et al. 2016 for AGNs with  $< 10^{42} \text{ erg s}^{-1}$  in the 14–195 keV band). It may be explained by considering that, in a very low luminosity (or Eddington ratio) AGN, gas in the torus or circumnuclear disk is depleted and star formation activity is quenched; this prevents the torus from being inflated and stops efficient mass transfer toward the SMBH, due to the lack of turbulence by supernova feedback (Kawakatu & Wada 2008).

## 5.3 Implications

To summarize these results, we have shown that the typical torus structure in RGs does not show any distinct differences from radio-quiet AGNs at the same Eddington ratios, at least in the range of  $-3 < \log \lambda_{\text{Edd}} < -1$  we have examined. Although we have to bear in mind that the sample size is limited to derive a conclusive argument, our work has two implications:

- (i) The torus structure is not an important factor that determines the presence or absence of powerful jets at  $-3 < \log \lambda_{\text{Edd}} < -1$ .
- (ii) The jets have physically little effects on the torus structure.

The first consequence can be understood if the launching mechanism of powerful jets is critically related to physics in the innermost region of the accretion disk (such as black hole spin and type of accretion flow) and is not determined solely by the Eddington ratio as discussed in Section 5.2. To check the second consequence (i.e., if radiation from the jet core could have significant impacts on the torus region), we refer to Meyer et al. (2011), who systematically studied the synchrotron peak luminosities ( $\log L_{\text{peak}}$ ) in radio-loud AGNs, including RGs and blazars. Since our objects are viewed through the obscuring tori, we can approximately use the observed jet luminosities as those actually irradiating the tori without corrections for relativistic beaming. Their figure 5 shows that FR II RGs have typically  $\log(L_{\text{peak}} \text{ erg s}^{-1}) \sim 44.5$  with a core dominance parameter (the ratio of the core luminosity to the total one including extended emission) of  $\log R_{\text{CE}} \sim -1.5$ . Thus, we can estimate the luminosities from the jet core in typical FR II RGs to be  $\sim 10^{43} \text{ erg s}^{-1}$ , which is much smaller than the AGN bolometric luminosities in our sample,  $\sim 10^{44-45} \text{ erg s}^{-1}$  (Figure 1). Hence, we infer that radiative feedback from the jet core can be neglected compared with that from the accretion disk even in an AGN with powerful jets.

## 6 CONCLUSION

We have reported the results of detailed broadband X-ray spectral analysis of the seven most radio-loud, X-ray obscured NLRGs in the *Swift*/BAT 70-month catalog, utilizing currently the highest-quality data observed with *Suzaku* and *NuSTAR*. The XCLUMPY model (Tanimoto et al. 2019) has been applied to the spectra, which enables us to constrain the torus covering fraction of each object. The main conclusions are summarized below.

- Most of our sample except Centaurus A cover a narrow range of AGN bolometric luminosities ( $44 < \log L_{\text{bol}} \text{ erg s}^{-1} < 45$ ) and Eddington ratios ( $-2 < \log \lambda_{\text{Edd}} < -1$ ), suggesting that the condition to launch powerful jets is not determined solely by the mass accretion rate or that normalized by the Eddington ratio.
- The relation between the Eddington ratio and the torus covering fraction of the RGs follows the same trend for radio-quiet AGNs obtained by Ricci et al. (2017b) based on a statistical analysis of obscured AGN fractions in a complete hard X-ray selected sample.



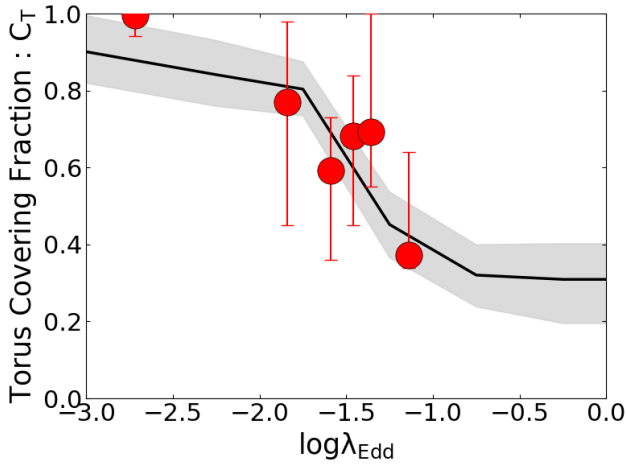


**Figure 3.** The torus covering fraction ( $C_T$ ) with  $\log N_H/\text{cm}^{-2} > 22$  as a function of Eddington ratio ( $\lambda_{\text{Edd}}$ ). The red circles represent our RG sample including Centaurus A (left-most, [Ogawa et al. 2021](#)). The relation obtained by [Ricci et al. \(2017b\)](#) for the *Swift*/BAT 70 month AGN sample is indicated by the black line (best-fit) and gray hatched area ( $1\sigma$  uncertainties). 3C 105, whose  $C_T$  is unconstrained by our data, is excluded in this plot.

This means that no distinct differences are found in the torus structure between AGNs with and without powerful jets.

- Our results suggest that the torus structure is not an important factor that determines the presence of jets. This is probably because the launching mechanism of jets is determined by physics in the innermost region of the accretion disk and is unrelated to distant torus structure. Also, AGN jets have physically little effects on the torus. In fact, estimated radiation luminosities from the jet core to the torus region are much smaller than those from the accretion disk.

## ACKNOWLEDGEMENTS

This work has been financially supported by JSPS KAKENHI Grant Numbers 20H01946 (Y.U.), 21J13894 (S.O.), 22J22795 (R.U.), and 22K20391 and 23K13154 (S.Y.). S.Y. is grateful for support from RIKEN Special Postdoctoral Researcher Program. C.R. acknowledges support from the Fondecyt Regular grant 1230345 and ANID BASAL project FB210003. We have made use of public data from Suzaku, which is obtained through the Data ARchives and Transmission System (DARTS) supplied by the Institute of Space and Astronautical Science (ISAS) at the Japan Aerospace Exploration Agency (JAXA), and NuSTAR Data Analysis Software (NuSTARDAS), which has been jointly developed by the Space Science Data Center (SSDC; ASI, Italy) and the Jet Propulsion Laboratory (JPL)/California Institute of Technology. We have also used NASA/IPAC Extragalactic Database (NED), which is operated by JPL/California Institute of Technology, under contract with NASA.

## DATA AVAILABILITY

The datasets generated and/or analysed in this study are available from the corresponding author on reasonable request.

## REFERENCES

Anders E., Grevesse N., 1989, *Geochimica Cosmochimica Acta*, **53**, 197

- Arnaud K. A., 1996, in *Jacoby G. H., Barnes J., eds, Astronomical Society of the Pacific Conference Series Vol. 101, Astronomical Data Analysis Software and Systems V*. p. 17
- Baloković M., et al., 2018, *ApJ*, **854**, 42
- Baumgartner W. H., Tueller J., Markwardt C. B., Skinner G. K., Barthelmy S., Mushotzky R. F., Evans P. A., Gehrels N., 2013, *ApJS*, **207**, 19
- Bottinelli L., Durand N., Fouque P., Garnier R., Gouguenheim L., Patrel G., Teerikorpi P., 1992, *A&AS*, **93**, 173
- Condon J. J., Helou G., Sanders D. B., Soifer B. T., 1996, *ApJS*, **103**, 81
- Condon J. J., Cotton W. D., Greisen E. W., Yin Q. F., Perley R. A., Taylor G. B., Broderick J. J., 1998, *AJ*, **115**, 1693
- Diez C. M., et al., 2023, *arXiv e-prints*, p. [arXiv:2303.09631](#)
- Elitzur M., Shlosman I., 2006, *ApJ*, **648**, L101
- Fabian A. C., 2012, *ARA&A*, **50**, 455
- Fanaroff B. L., Riley J. M., 1974, *MNRAS*, **167**, 31P
- Fioretti V., Angelini L., Mushotzky R. F., Koss M., Malaguti G., 2013, *A&A*, **555**, A44
- Fukazawa Y., et al., 2009, *PASJ*, **61**, S17
- Fukumura K., Kazanas D., Contopoulos I., Behar E., 2010, *ApJ*, **715**, 636
- George I. M., Fabian A. C., 1991, *MNRAS*, **249**, 352
- Hardcastle M. J., Alexander P., Pooley G. G., Riley J. M., 1999, *MNRAS*, **304**, 135
- Harrison F. A., et al., 2013, *ApJ*, **770**, 103
- Hitomi Collaboration et al., 2018, *PASJ*, **70**, 13
- Ikeda S., Awaki H., Terashima Y., 2009, *ApJ*, **692**, 608
- Ishisaki Y., et al., 2007, *PASJ*, **59**, 113
- Jones D. H., et al., 2009, *MNRAS*, **399**, 683
- Kataoka J., et al., 2007, *PASJ*, **59**, 279
- Kawakatu N., Wada K., 2008, *ApJ*, **681**, 73
- Kawamuro T., Ueda Y., Tazaki F., Terashima Y., Mushotzky R., 2016, *ApJ*, **831**, 37
- Kim M., Barth A. J., Ho L. C., Son S., 2021, *ApJS*, **256**, 40
- Kormendy J., Ho L. C., 2013, *ARA&A*, **51**, 511
- Koss M. J., et al., 2022, *ApJS*, **261**, 2
- Kuźmicz A., Jamroz M., Bronarska K., Janda-Boczar K., Saikia D. J., 2018, *ApJS*, **238**, 9
- LaMassa S. M., Yaqoob T., Tzanavaris P., Gandhi P., Heckman T., Lansbury G., Siemiginowska A., 2023, *ApJ*, **944**, 152
- Larsson J., Fabian A. C., Ballantyne D. R., Miniutti G., 2008, *MNRAS*, **388**, 1037
- Lohfink A. M., et al., 2015, *ApJ*, **814**, 24
- Lohfink A. M., et al., 2017, *ApJ*, **841**, 80
- Loveday J., Peterson B. A., Maddox S. J., Efstathiou G., 1996, *ApJS*, **107**, 201
- Madsen K. K., Beardmore A. P., Forster K., Guainazzi M., Marshall H. L., Miller E. D., Page K. L., Stuhlinger M., 2017, *AJ*, **153**, 2
- Magdziarz P., Zdziarski A. A., 1995, *MNRAS*, **273**, 837
- Marconi A., Risaliti G., Gilli R., Hunt L. K., Maiolino R., Salvati M., 2004, *MNRAS*, **351**, 169
- Meyer E. T., Fossati G., Georganopoulos M., Lister M. L., 2011, *ApJ*, **740**, 98
- Mitsuda K., et al., 2007, *PASJ*, **59**, S1
- Miyaji T., et al., 2019, *ApJ*, **884**, L10
- Miyakawa T., Ebisawa K., Inoue H., 2012, *PASJ*, **64**, 140
- Murphy K. D., Yaqoob T., 2009, *MNRAS*, **397**, 1549
- Odaka H., Aharonian F., Watanabe S., Tanaka Y., Khangulyan D., Takahashi T., 2011, *ApJ*, **740**, 103
- Odaka H., Yoneda H., Takahashi T., Fabian A., 2016, *MNRAS*, **462**, 2366
- Ogawa S., Ueda Y., Tanimoto A., Yamada S., 2021, *ApJ*, **906**, 84
- Owen F. N., Laing R. A., 1989, *MNRAS*, **238**, 357
- Panagiotou C., Walter R., 2020, *A&A*, **640**, A31
- Ramos Almeida C., Ricci C., 2017, *Nature Astronomy*, **1**, 679
- Reynolds C. S., et al., 2015, *ApJ*, **808**, 154
- Ricci C., et al., 2017a, *ApJS*, **233**, 17
- Ricci C., et al., 2017b, *Nature*, **549**, 488
- Ricci C., et al., 2018, *MNRAS*, **480**, 1819
- Ricci C., et al., 2022, *ApJ*, **938**, 67
- Sambruna R. M., et al., 2009, *ApJ*, **700**, 1473

- Sambruna R. M., Tombesi F., Reeves J. N., Braito V., Ballo L., Gliozzi M., Reynolds C. S., 2011, *ApJ*, 734, 105
- Sikora M., Stawarz L., Lasota J.-P., 2007, *ApJ*, 658, 815
- Spinrad H., Djorgovski S., Marr J., Aguilar L., 1985, *PASP*, 97, 932
- Tanaka Y., et al., 1995, *Nature*, 375, 659
- Tanimoto A., Ueda Y., Odaka H., Kawaguchi T., Fukazawa Y., Kawamuro T., 2019, *ApJ*, 877, 95
- Tanimoto A., Ueda Y., Odaka H., Ogawa S., Yamada S., Kawaguchi T., Ichikawa K., 2020, *ApJ*, 897, 2
- Tanimoto A., Ueda Y., Odaka H., Yamada S., Ricci C., 2022, *ApJS*, 260, 30
- Tazaki F., Ueda Y., Ishino Y., Eguchi S., Isobe N., Terashima Y., Mushotzky R. F., 2010, *ApJ*, 721, 1340
- Tazaki F., Ueda Y., Terashima Y., Mushotzky R. F., 2011, *ApJ*, 738, 70
- Tazaki F., Ueda Y., Terashima Y., Mushotzky R. F., Tombesi F., 2013, *ApJ*, 772, 38
- Terashima Y., Wilson A. S., 2003, *ApJ*, 583, 145
- Tombesi F., Tazaki F., Mushotzky R. F., Ueda Y., Cappi M., Gofford J., Reeves J. N., Guainazzi M., 2014, *MNRAS*, 443, 2154
- Ueda Y., Akiyama M., Hasinger G., Miyaji T., Watson M. G., 2014, *ApJ*, 786, 104
- Uematsu R., Ueda Y., Tanimoto A., Kawamuro T., Setoguchi K., Ogawa S., Yamada S., Odaka H., 2021, *ApJ*, 913, 17
- Ursini F., Bassani L., Panessa F., Bazzano A., Bird A. J., Malizia A., Ubertini P., 2018a, *MNRAS*, 474, 5684
- Ursini F., et al., 2018b, *MNRAS*, 481, 4250
- Wada K., 2015, *ApJ*, 812, 82
- Wagner A. Y., Bicknell G. V., Umemura M., 2012, *ApJ*, 757, 136
- White R. L., Becker R. H., 1992, *ApJS*, 79, 331
- Willingale R., Starling R. L. C., Beardmore A. P., Tanvir N. R., O'Brien P. T., 2013, *MNRAS*, 431, 394
- Yamada S., Ueda Y., Tanimoto A., Imanishi M., Toba Y., Ricci C., Privon G. C., 2021, *ApJS*, 257, 61

## APPENDIX A: COMPARISON OF SPECTRAL FITTING RESULTS WITH PREVIOUS WORKS

In this section, we compare our spectral fitting results with those reported in the literature for each object. Since various spectral models were used in the literature, we focus on two basic continuum parameters, the photon index of the intrinsic power-law component ( $\Gamma$ ) and the line-of-sight hydrogen column density ( $N_{\text{H}}^{\text{LOS}}$ ), to roughly check the consistency with our results. Ricci et al. (2017a) (hereafter R17) analyzed the broadband (0.3–150 keV) spectra of 838 AGNs including our sample by utilizing the *Swift*/BAT 70-month spectra and soft X-ray data available then. They basically adopted the *PEXRAV* model to represent the reflection component. We note that Tombesi et al. (2014) analyzed the same *Suzaku* data of all objects but VII Zw 292. We do not refer to the continuum parameters summarized in their Table B2, however, because only the 3.5–10.5 keV band spectra were utilized to search for UFO features.

### A1 PKS 0326–288

The analysis results of the *NuSTAR* data are reported in this paper for the first time. We obtain  $\Gamma = 1.74^{+0.13}_{-0.14}$  and  $N_{\text{H}}^{\text{LOS}} = 49.7^{+3.5}_{-6.79} \times 10^{22} \text{cm}^{-2}$ . These values are consistent with those of R17 using the *Swift*/XRT and *Swift*/BAT data ( $\Gamma = 2.12^{+0.4}_{-0.5}$  and  $N_{\text{H}}^{\text{LOS}} = 38.0^{+62.0}_{-17.1} \times 10^{22} \text{cm}^{-2}$ ).

### A2 VII Zw 292

The *Suzaku* results are reported here for the first time. We obtain  $\Gamma = 1.36^{+0.14}_{-0.13}$  and  $N_{\text{H}}^{\text{LOS}} = 41.14^{+2.71}_{-2.49} \times 10^{22} \text{cm}^{-2}$ . Using the

*XMM-Newton*/pn and *Swift*/BAT data, R17 obtained  $\Gamma = 1.52^{+0.52}_{-0.47}$  and  $N_{\text{H}}^{\text{LOS}} = 61.7^{+38.3}_{-19.0} \times 10^{22} \text{cm}^{-2}$ . Similarly, Ursini et al. (2018a) obtained  $\Gamma = 1.61 \pm 0.17$  and  $N_{\text{H}}^{\text{LOS}} = 40 \pm 8 \times 10^{22} \text{cm}^{-2}$  from the *XMM-Newton*/pn, *Swift*/BAT, and *NuSTAR* data. These results are consistent with ours.

### A3 3C 403

We obtain  $\Gamma = 1.87^{+0.19}_{-0.24}$  and  $N_{\text{H}}^{\text{LOS}} = 43.65^{+7.1}_{-6.71} \times 10^{22} \text{cm}^{-2}$ . These values agree with those of R17 ( $\Gamma = 1.69^{+0.14}_{-0.13}$  and  $N_{\text{H}}^{\text{LOS}} = 49.0^{+17.1}_{-4.3} \times 10^{22} \text{cm}^{-2}$ ) based on the *Swift*/XRT and *Swift*/BAT data within the errors. Fitting the same *NuSTAR* spectra as ours with the *PEXRAV* model, Panagiotou & Walter (2020) obtained  $\Gamma = 1.71^{+0.09}_{-0.28}$ , and  $N_{\text{H}}^{\text{LOS}} = 34.6^{+3.2}_{-5.3} \times 10^{22} \text{cm}^{-2}$ , which are consistent with our results. However, Tazaki et al. (2011) obtained a somewhat flatter slope,  $\Gamma = 1.53^{+0.03}_{-0.02}$ , and  $N_{\text{H}}^{\text{LOS}} = 61^{+6}_{-5} \times 10^{22} \text{cm}^{-2}$ , by fitting the *Suzaku* and *Swift*/BAT spectra with an analytic model including *PEXRAV*. We infer that it may be due to possible spectral variability between the *NuSTAR* and *Suzaku* observation epochs as indicated by the very small value of the time-variability constant (0.22, Table 3).

### A4 3C 105

We obtain  $\Gamma = 1.48^{+0.12}_{-0.12}$  and  $N_{\text{H}}^{\text{LOS}} = 39.27^{+2.97}_{-3.58} \times 10^{22} \text{cm}^{-2}$ . These values are consistent with those of R17 based on the *XMM-Newton*/pn and *Swift*/BAT spectra ( $\Gamma = 1.29^{+0.31}_{-0.29}$  and  $N_{\text{H}}^{\text{LOS}} = 43.7^{+7.6}_{-5.6} \times 10^{22} \text{cm}^{-2}$ ). Fioretti et al. (2013) obtained  $\Gamma = 1.78^{+0.2}_{-0.19}$  and  $N_{\text{H}}^{\text{LOS}} = 45.96^{+6.24}_{-6.56} \times 10^{22} \text{cm}^{-2}$  using *Suzaku* and *Swift*/BAT data, which are also consistent with ours.

### A5 3C 452

Our best-fit values,  $\Gamma = 1.61^{+0.06}_{-0.07}$  and  $N_{\text{H}}^{\text{LOS}} = 43.39^{+2.24}_{-5.78} \times 10^{22} \text{cm}^{-2}$ , are consistent with Fioretti et al. (2013), who obtained  $\Gamma = 1.55^{+0.14}_{-0.11}$  and  $N_{\text{H}}^{\text{LOS}} = 43.52^{+10.85}_{-6.92} \times 10^{22} \text{cm}^{-2}$  using *Suzaku* and *Swift*/BAT data. Panagiotou & Walter (2020) analyzed the same *NuSTAR* spectra as ours and derived  $N_{\text{H}}^{\text{LOS}} = 46.8 \pm 2.3 \times 10^{22} \text{cm}^{-2}$  with the *PEXRAV* model by fixing  $\Gamma$  at 1.73. This value is consistent with ours. Using the *XMM-Newton*/pn and *Swift*/BAT data, R17 reported a flatter slope and a larger absorption ( $\Gamma = 1.31^{+0.2}_{-0.18}$  and  $N_{\text{H}}^{\text{LOS}} = 57.5^{+10.1}_{-9.7} \times 10^{22} \text{cm}^{-2}$ ) than our results. This is most likely due to time variability between the *XMM-Newton* and *Suzaku* observations, because we find that soft X-ray flux below  $\sim 3$  keV was significantly lower in the former epoch than in the latter one.

### A6 PKS 2356–61

Our results ( $\Gamma = 1.58^{+0.05}_{-0.01}$  and  $N_{\text{H}}^{\text{LOS}} = 13.64^{+0.56}_{-0.34} \times 10^{22} \text{cm}^{-2}$ ) are consistent with those of R17 obtained from the *Suzaku* and *Swift*/BAT data ( $\Gamma = 1.59^{+0.13}_{-0.16}$  and  $N_{\text{H}}^{\text{LOS}} = 14.5^{+0.7}_{-0.7} \times 10^{22} \text{cm}^{-2}$ ). Using the same *NuSTAR* data as ours and the *Swift*/BAT data, Ursini et al. (2018b) obtained  $\Gamma = 1.7 \pm 0.3$  and  $N_{\text{H}}^{\text{LOS}} = 14 \pm 5 \times 10^{22} \text{cm}^{-2}$ , which are also consistent with our results. Panagiotou & Walter (2020) also analyzed the same *NuSTAR* data and obtained  $\Gamma = 1.41 \pm 0.27$  and  $N_{\text{H}}^{\text{LOS}} = 12.5^{+4.3}_{-4.2} \times 10^{22} \text{cm}^{-2}$  by applying the *PEXRAV* model. These values are in good agreement with ours.

This paper has been typeset from a  $\text{\LaTeX}$  file prepared by the author.